Toward Optimal Heat Transfer of 2D–3D Heterostructures via van der Waals Binding Effects

Toward optimal heat transfer of 2D-3D heterostructures via van der Waals binding effects

Manuscript for *ACS Applied Materials & Interfaces*

Lenan Zhang[†, #], Yang Zhong[†, #], Xin Qian[†], Qichen Song[†], Jiawei Zhou[†], Long Li[‡], Liang Guo[*, ‡], Gang Chen[*, †], Evelyn N. Wang[*, †]

[†] Department of Mechanical Engineering, Massachusetts Institute of Technology, Cambridge, Massachusetts 02139, United States

[‡] Department of Mechanical and Energy Engineering, Southern University of Science and Technology, Shenzhen 518055, China

[*] Corresponding authors: guol3@sustech.edu.cn, gchen2@mit.edu, and enwang@mit.edu

[#] Equal contribution to this work

ABSTRACT (< 150 WORDS)

Two-dimensional (2D) materials and their heterogeneous integration have enabled promising electronic and photonic applications. However, significant thermal challenges arise due to numerous van der Waals (vdW) interfaces limiting dissipation of heat generated in the device. In this work, we investigate the vdW binding effect on heat transport through an MoS_2-amorphous silica heterostructure. We show using atomistic simulations that the cross-plane thermal conductance starts to saturate with the increase of vdW binding energy, which is attributed to substrate induced localized phonons. With these atomistic insights, we perform device-level heat transfer optimizations. Accordingly, we identify a regime, characterized by the coupling of in-plane and cross-plane heat transport mediated by the vdW binding energy, where maximal heat dissipation in the device is achieved. These results elucidate fundamental heat transport through the vdW heterostructure and provide a pathway toward optimizing thermal management in 2D nanoscale devices.

KEYWORDS: 2D-3D heterostructure, van der Waals, thermal conductance, thermal conductivity, MoS_2, phonon

INTRODUCTION

Advances in two-dimensional (2D) materials and their heterogeneous integration with three-dimensional (3D) substrates (2D-3D heterostructures) offer great opportunities for next-generation nanoscale electronic and photonic devices,[1,2] including field-effect transistors,[3–5] spintronics,[6,7] solar cells,[8,9] and light emitters.[10,11] However, the high thermal resistance due to the presence of numerous interfaces bonded by the weak van der Waals (vdW) interaction limits the energy dissipation,[12,13] induces significant temperature rise,[14,15] creates large thermal mismatch,[16,17] and therefore degrades the device performance. Although this high thermal resistance has been confirmed by recent experimental characterizations[14,18–20] and numerical simulations,[21–23] strategies to enhance heat transfer through 2D-3D heterostructures have yet to be developed. Meanwhile, it has been shown that electrical and optical properties of 2D-3D heterostructures can be engineered through the vdW interaction, where the vdW binding can be tuned by applying pressure,[24–28] strain,[29] voltage,[30] doping level,[31] and surface chemistry.[32] In particular, recently, it has been experimentally demonstrated that a large tunability of the vdW interaction can be achieved by applying extreme pressure,[33] which leads to a drastic change of interfacial thermal transport properties and holds significant promises for device-level thermal management. However, fundamental understanding of how vdW binding affects the overall thermal transport of 2D-3D heterostructure is limited, and practical considerations of how the atomistic level insights guide device-level thermal optimization remains elusive.

Here, we investigate thermal transport through an MoS_2-amorphous silica (a-SiO_2) heterostructure. Although the thermal resistance of 2D-3D interfaces is not necessarily always

higher than that of the covalently bonded 3D-3D interfaces, the heterogeneous integration of a 2D film and 3D substrate through vdW interaction leads to distinct anisotropic thermal transport. Hence, in this work, vdW binding effects on both the in-plane and cross-plane heat transfer are considered. Previous understanding of substrate effects on 2D film thermal transport mainly focused on the weak vdW interaction regime around the intrinsic vdW coupling strength. The anisotropic thermal transport of 2D-3D heterostructure spanning a broad range of vdW binding was not systematically studied. Using atomistic simulations, we show that the in-plane thermal conductivity decreases while the cross-plane thermal conductance increases with the increase of vdW binding energy. This result can be explained *via* examining the phonon relaxation time. In particular, a saturating trend of the cross-plane thermal conductance is observed at high vdW binding energy, which is a result of localized phonons in the MoS_2 monolayer due to the presence of the amorphous 3D substrate. The insights gained from our atomistic level analysis were then translated to device-level thermal optimizations. Given the opposite trends of in-plane thermal conductivity and cross-plane thermal conductance, an optimal vdW binding energy corresponding to the minimum thermal resistance of the 2D-3D heterostructure exists. Furthermore, we show that three characteristic lengths, *i.e.*, the hotspot size, 2D film size, and lateral heat spread length, determine the device-level thermal transport and the optimal vdW binding energy. Our study fills an important knowledge gap about how the vdW binding affects the thermal transport through the 2D-3D heterostructure, bridging heat transfer at the atomistic level and the device-level. The results offer insights to maximize heat dissipation of high-performance 2D nanoscale devices.

RESULTS AND DISCUSSION

Figure 1 shows the overall heat transfer through a 2D-3D heterostructure, where a 2D film is supported by a 3D bulk substrate. A hotspot, which is commonly seen during electronic device operation is created within the 2D film due to the highly localized heat generation. Energy dissipation involves both the in-plane and cross-plane heat transfer (Figure 1), which are characterized by the in-plane thermal conductivity k of the 2D film and the cross-plane thermal conductance G between the 2D film and the 3D substrate, respectively. Sufficient in-plane heat transfer due to the high k is important to the lateral heat spreading and therefore reducing the peak temperature of the hotspot. Meanwhile, the cross-plane heat transfer determines how much heat can be rejected from the 2D film to the bulk substrate and then dissipated into the environment. To understand the effect of vdW binding on both the in-plane and cross-plane thermal transport, we considered an example 2D-3D heterostructure consisting of a MoS_2 monolayer and an a-SiO_2 substrate (dashed box of Figure 1), which is representative for the device-level applications.[15]

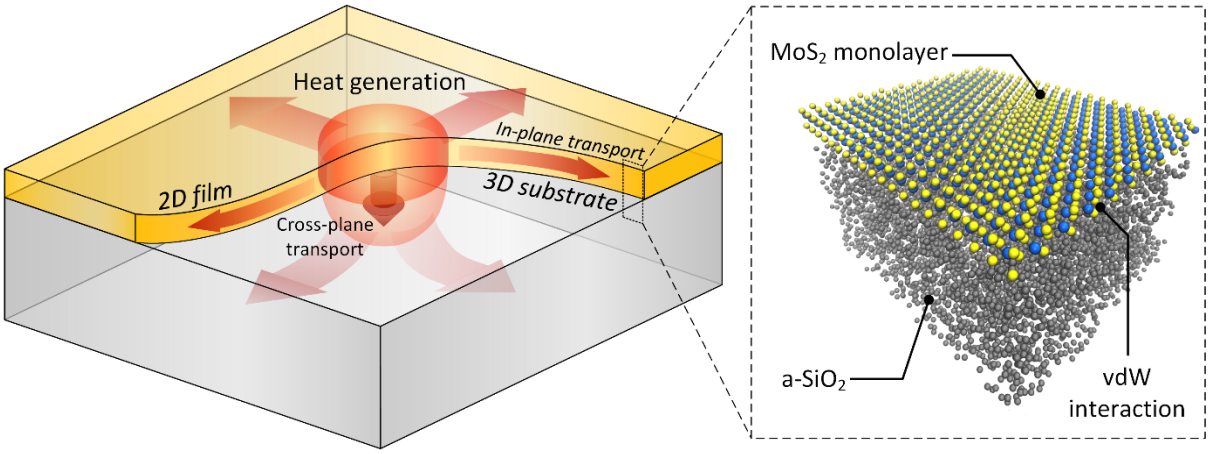

Figure 1. Schematic of the overall heat transfer through a 2D-3D heterostructure with localized heat generation. Both the in-plane and cross-plane heat transfer occur, which are determined

by the in-plane thermal conductivity k and the cross-plane thermal conductance G, respectively. k and G vary with the vdW binding energy. Dashed box: atomistic structure of a representative 2D-3D heterostructure consisting of MoS_2 and a-SiO_2.

The thermal transport properties (k and G) of the MoS_2-a-SiO_2 heterostructure were calculated by molecular dynamics (MD) simulation using the LAMMPS package.[34] The interatomic interactions of the MoS_2 monolayer and the a-SiO_2 substrate were modeled by a modified Stillinger-Weber potential[35] and the Tersoff potential,[36] respectively (see Supporting Information S1-S4 for details about the MD simulation). The interaction between the MoS_2 monolayer and the a-SiO_2 substrate is assumed to be of vdW type,[22] which can be modeled by the Lennard-Jones (LJ) potential u,

$$u(r) = 4\varepsilon' \left[\left(\frac{\sigma}{r}\right)^{12} - \left(\frac{\sigma}{r}\right)^{6} \right] \quad (1)$$

where r and σ are the interatomic distance and distance parameter for the atom pairs Mo-Si, Mo-O, S-Si, and S-O (see Supporting Information S2 for the values of σ for different atom pairs), respectively. ε' is the binding energy parameter which can be tuned in this work. We described vdW binding energy by scaling ε' with respect to the reference binding energy ε, which is given by the universal force field (UFF)[37] and represents the intrinsic binding strength of the MoS_2-a-SiO_2 vdW interface (see Supporting Information S2 for the values of ε for different atom pairs). Note that the polar characteristics were not considered when modeling the interaction between the MoS_2 monolayer and a-SiO_2 substrate. By comparing with the experimental data,[19] it has been shown that this vdW type assumption can provide reasonable

prediction for the interfacial thermal transport through the MoS_2-a-SiO_2 heterostructure.[22] The effects of polar characteristics on the thermal transport of 2D-3D heterostructures require further in-depth investigations.

Figure 2a and 2b show k and G as a function of the dimensionless binding energy ε'/ε ranging from one to 25, respectively. The in-plane thermal conductivity of MoS_2 monolayer was calculated using the Green-Kubo method *via* the equilibrium MD (EMD) simulation at 300 K (see Supporting Information S1 for details).[38–40] For the a-SiO_2 supported MoS_2, the value of k monotonically decreases with ε'/ε, which can be well described by an exponential decay (*i.e.*, $k = 8.5 + 96 \times exp(-0.32\ \varepsilon'/\varepsilon)$ W/(mK), the red-solid line in Figure 2a). This exponential decay was also reported by a very recent work in the weak vdW binding energy regime ($\varepsilon'/\varepsilon \leqslant 3$).[41] The uncertainty of k was determined by the standard deviation from multiple simulations (see Supporting Information S1 for details). The inset of Figure 2a shows the vdW interaction between a representative S-O atom pair. We also calculated the in-plane thermal conductivity of a free-standing MoS_2 monolayer (*i.e.*, k =163±49 W/(mK) at $\varepsilon'/\varepsilon = 0$ in Figure 2a), which shows reasonable agreement with literature data.[40,42–44]

The cross-plane thermal conductance between the MoS_2 monolayer and a-SiO_2 substrate was calculated with a thermal circuit approach using the approach-to-equilibrium MD (see Supporting Information S3 for details).[22,45] A 200 K temperature rise was created between the MoS_2 and a-SiO_2 that were initially thermally equilibrated at 300 K. The value of G can be obtained by fitting the temperature decay with time through a thermal RC circuit with the heat capacity of MoS_2 (C_{MoS2}) and a-SiO_2 (C_{SiO2}) as the input (see inset of Figure 2b and Supporting

Information S3 for details). The values of heat capacity were determined from the same simulated material systems (see Supporting Information S1 for details). The uncertainty of each data point is the standard deviation of five simulations. Note that this thermal circuit approach by "directly heating" the MoS_2 depicts the process of heat transfer from the MoS_2 to the substrate, which is similar to actual device operating conditions.[14,15] Figure 2b shows that G increases with ε'/ε. When $\varepsilon'/\varepsilon < 10$, G is linearly related to ε'/ε due to the increase of interfacial coupling strength (yellow-dashed line in Figure 2b). However, a nonlinear behavior was observed when $\varepsilon'/\varepsilon > 10$, where G increases with ε'/ε more slowly and shows a saturating trend. The overall behavior of cross-plane thermal conductance due to the vdW binding effect can be well-described by a quadratic fitting (*i.e.*, $G = -0.17(\varepsilon'/\varepsilon)^2 + 10.2\ \varepsilon'/\varepsilon - 5.6$ (MW/(m^{2}K)), the red-solid line in Figure 2b). Note that a similar saturating trend of cross-plane thermal transport was observed in a recent experiment with MoS_2 multilayers under high pressure.[33] These results suggest that although our simulation is based on an empirical potential from the UFF and the specific values of the calculated thermal properties can be less accurate, our analysis is capable of capturing the general trend and dominant physics due to vdW binding effects. Therefore, it is essential to further investigate thermal transport of 2D-3D heterostructure in the strong vdW interaction regime and elucidate the underlying mechanisms.

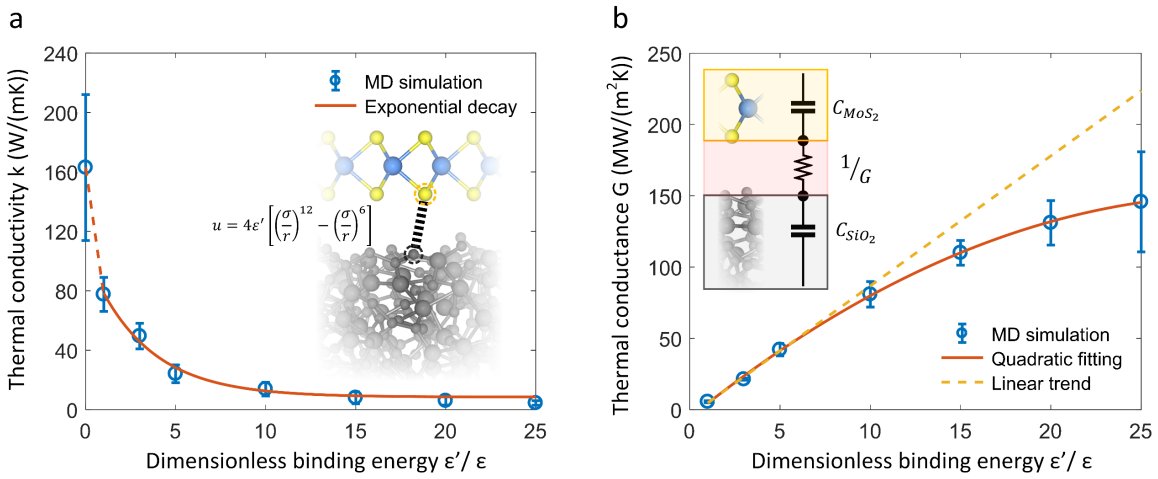

Figure 2. (a) In-plane thermal conductivity of MoS_2 monolayer as a function of vdW binding energy. (b) Cross-plane thermal conductance between the MoS_2 monolayer and a-SiO_2 substrate as a function of vdW binding energy. Inset of (a): interaction between the MoS_2 and a-SiO_2 modeled by the LJ potential. Inset of (b): thermal RC circuit used for determining the cross-plane thermal conductance.

To understand the behavior of thermal transport properties, especially the saturating trend of cross-plane thermal conductance due to the vdW binding energy, we performed phonon mode analysis.[46–48] By calculating the heat flux correlation as a function of frequency (Figure S8 in Supporting Information S5), we showed that the high frequency peaks of heat flux correlation, which have similar frequencies to those of the high frequency acoustic phonons or even the optical phonons of MoS_2, become significant with the increase of ε'/ε, indicating all of the phonon modes need to be considered.

We first studied the effect of vdW binding on phonon relaxation time. Figure 3a shows a map of the phonon relaxation time for two select branches of acoustic and optical phonons in the

first Brillouin zone (BLZ) of MoS_2 (see Supporting Information S1 for details), where the lattice structure of MoS_2 and its primitive vectors ($\boldsymbol{a}_1$ and $\boldsymbol{a}_2$) are shown in Figure 3b, which defines the 2D BLZ of MoS_2 (Figure 3c). We sampled the phonon relaxation time τ of 81 **k**-points uniformly distributed in the first quadrant of 2D BLZ using spectral energy density (SED) analysis.[49,50] With the increase of ε'/ε (especially when $\varepsilon'/\varepsilon < 10$), the relaxation time for most of the phonon modes in the 2D BLZ decreases, which can be explained by the destruction of long-range order of phonon transport due to stronger interfacial scattering. Since $k \propto \tau$ according to phonon gas theory,[48] the decrease of k with ε'/ε shown in Figure 2a can thus be explained. On the other hand, for the cross-plane phonon transport, there is an intrinsic dimensional mismatch between the 2D MoS_2 and 3D a-SiO_2, because phonons in the MoS_2 do not contain the wavevector k_z and group velocity v_z components that are perpendicular to the interface (*i.e.*, along the z-direction). For this reason, scattering due to the vdW interaction at the 2D-3D interface creates phonons in the a-SiO_2 with a z-direction group velocity and therefore facilitates the cross-plane thermal transport. A similar coupling mechanism between the 2D film and 3D substrate was also identified by Feng *et al*. in a graphene-silicon heterostructure.[51] Since the phonon scattering rate $\Gamma = \tau^{-1}$, Γ increases with ε'/ε, which explains the increase of G observed in Figure 2b.

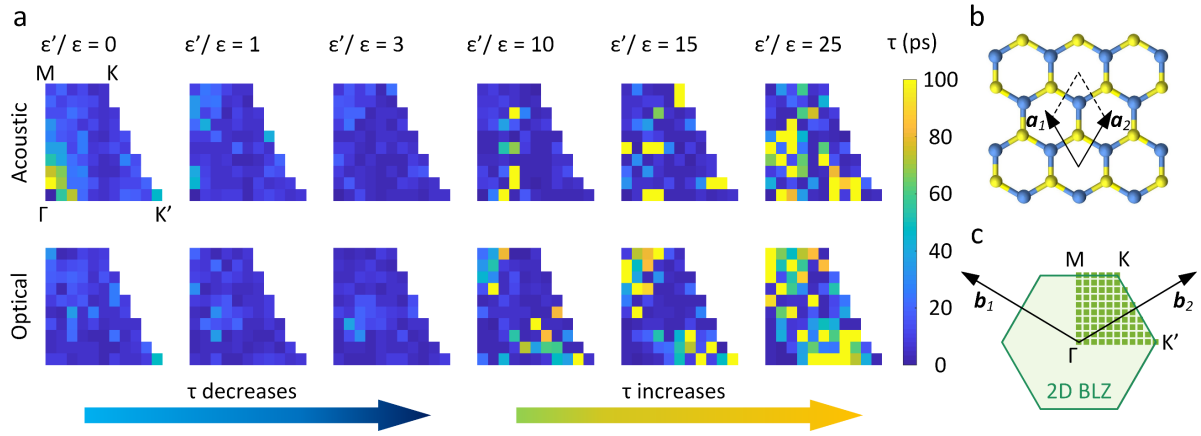

Figure 3. (a) First BLZ phonon relaxation time map for the acoustic and optical branches under different vdW binding energies. A few modes with very long relaxation time (τ > 100 ps, marked by the bright yellow in the scale bar) were observed when $\varepsilon'/\varepsilon \geqslant 10$. (b) Lattice structure and the corresponding primitive vectors of MoS_2 monolayer. The blue arrow indicates that τ decreases with ε'/ε for most of the phonon modes especially when $\varepsilon'/\varepsilon < 10$. The yellow arrow indicates that the number of long relaxation time modes increases when $\varepsilon'/\varepsilon > 10$. (c) Schematic of the 2D BLZ of MoS_2 monolayer. The 81 green squares in the first quadrant of 2D BLZ indicate the corresponding **k** points used for the relaxation time analysis in (a).

When $\varepsilon'/\varepsilon = 10$, although there is still a suppression of relaxation time for most of phonon modes, a few unexpected long relaxation time phonons ($\tau > 50$ ps) were observed. The number of long relaxation time phonons increases with ε'/ε and becomes significant when $\varepsilon'/\varepsilon = 25$ (Figure 3a). Due to the presence of these long relaxation time phonons, the trend for the decrease of k and the increase of G becomes slower with the increase of ε'/ε, which finally leads to the saturating trend of both k and G at a sufficiently large ε'/ε as shown in Figure 2. Figure 4a-c shows the phonon relaxation time as a function of phonon frequency for $\varepsilon'/\varepsilon = 1$,

ε'/ε = 3, and ε'/ε = 15, respectively. Compared with the phonon relaxation time of a free-standing MoS_2 monolayer (dark-grey points), a general suppression of phonon relaxation time with the increase of ε'/ε (red points) is shown, which agrees with the phonon relaxation time map in the 2D BLZ (Figure 3a). The long relaxation time phonons, which first appear in the high frequency optical mode (Figure 4a and 4b), gradually becomes significant for both the optical and acoustic modes (Figure 4c) with the increase of ε'/ε. More interestingly, we compared the phonon relaxation time with the vdW force spectrum, which was extracted from the Fourier transform of the time-domain vdW force in the MD simulation (see Supporting Information S5 for details). We used this approach to partially explain the uncommon long relaxation time phonons in the large vdW binding regime. The three distinct peaks for the long relaxation time phonons around 5 THz, 10 THz, and 13.5 THz are highly consistent with the peaks shown in the vdW force spectrum (Figure 4c), indicating a strong interrelationship between the long relaxation time phonons and vdW interaction.

To further understand the mechanism of long relaxation time phonons, we analyzed the phonon eigenvectors and calculated the phonon participation ratio for the MoS_2-a-SiO_2 heterostructure using the lattice dynamics (LD). LD calculations were performed using GULP (see Supporting Information S6 for details).[52] Propagating phonon modes were commonly seen in the free-standing MoS_2, where the eigenvectors of two representative propagating modes were shown in Figure 4d and 4e, respectively. However, when the MoS_2 monolayer is supported by the a-SiO_2 substrate, highly localized phonon modes with eigenvectors confined in a small region of MoS_2 atoms were observed in the heterostructure (Figure 4f and 4g). Since these localized phonons do not propagate in the material and weakly interact with other phonons, they have

limited contribution to the thermal transport.[53,54] To quantify these localized modes, we calculated the phonon participation ratio γ for all phonon modes in the MoS_2-a-SiO_2 heterostructure (Figure 4h), where γ of localized modes is typically smaller than 0.1.[47,53–55] Figure 4h shows that most of localized phonons come from the MoS_2 monolayer (red points), which was determined by the atom position of the largest eigenvector for a localized phonon mode (see Supporting Information S6 for details). Two representative phonon modes localized in MoS_2 (corresponding to the yellow and purple circles in Figure 4h) are visualized in Figure 4f and 4g, respectively, where the large eigenvector components are localized in MoS_2 as marked by the yellow and purple circles. More importantly, these localized phonons also mainly occur at around 5 THz, 10 THz, and 13.5 THz (Figure 4h), which agrees with the distribution of long relaxation time phonons shown in Figure 4c. Therefore, the long relaxation time phonons can be explained by the vdW interaction induced localized phonons, which weakly interact with other modes and therefore lead to the slower decrease of k and saturating trend of G. In addition, we also analyzed the phonon group velocity $\boldsymbol{v}$ and phonon density of state (PDOS) of the MoS_2-a-SiO_2 heterostructure for different vdW binding energy (see Figure S10 and S11 in Supporting Information S7), which provides more information about the phonon characteristics due to vdW interaction and further supports the results shown in Figure 2.

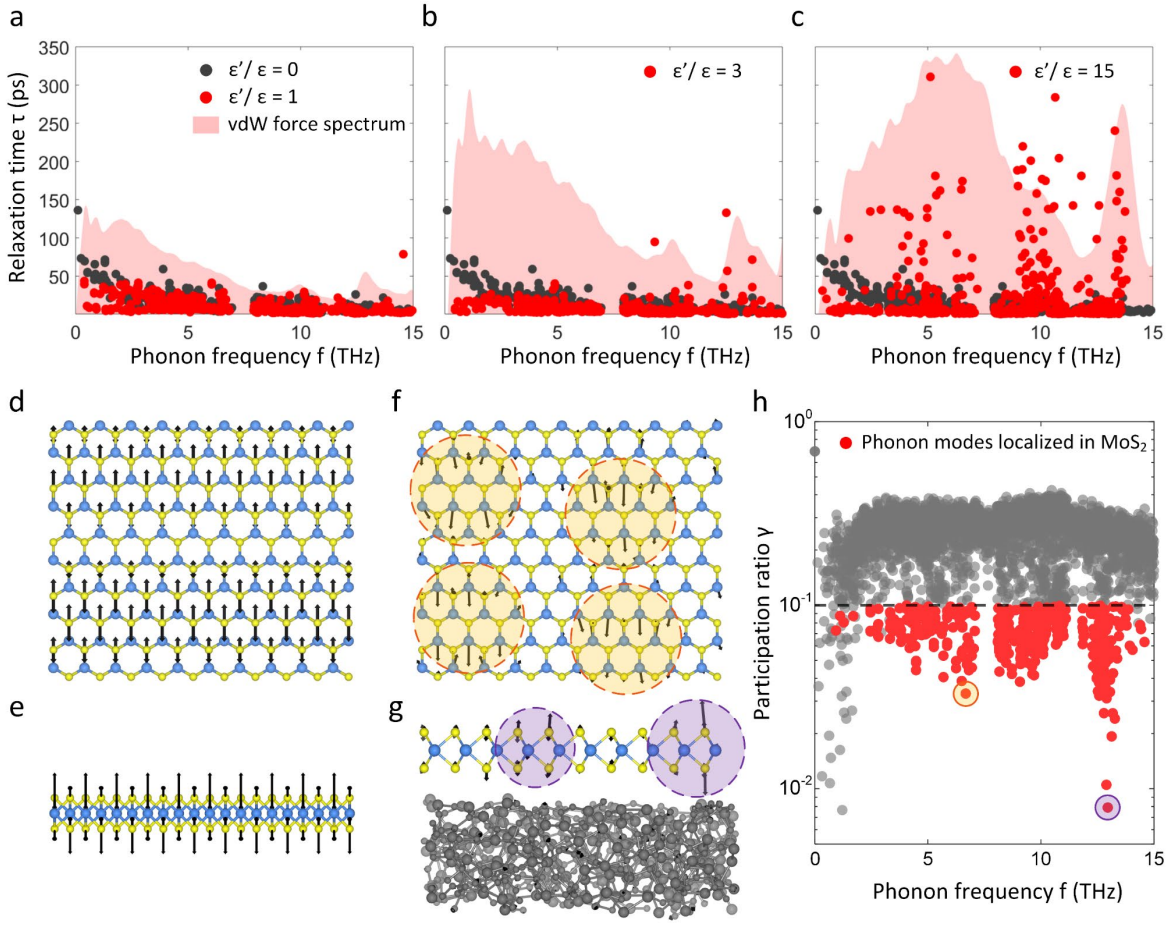

Figure 4. Phonon relaxation time as a function of phonon frequency when (a) $\varepsilon'/\varepsilon = 1$, (b) $\varepsilon'/\varepsilon = 3$, and (c) $\varepsilon'/\varepsilon = 15$. Red shadows: the corresponding vdW force spectrum when (a) $\varepsilon'/\varepsilon = 1$, (b) $\varepsilon'/\varepsilon = 3$, and (c) $\varepsilon'/\varepsilon = 15$. The amplitude of the vdW force spectrum is in arbitrary units. (d) Top view of eigenvectors of a representative propagating phonon mode with 8.40 THz phonon frequency in a free-standing MoS_2 monolayer. (e) Side view of eigenvectors of a representative propagating phonon mode with 5.71 THz phonon frequency in a free-standing MoS_2 monolayer. (f) Top view of eigenvectors of a representative localized phonon mode with 6.68 THz phonon frequency in the MoS_2-a-SiO_2 heterostructure. Yellow dashed circles: eigenvectors confined in the small regions of MoS_2 atoms. (g) Side view of eigenvectors of a representative localized phonon mode with 12.96 THz phonon frequency in the MoS_2-a-SiO_2

heterostructure. Purple dashed circles: eigenvectors confined in the small regions of MoS_2 atoms. (h) Phonon participation ratio of the MoS_2-a-SiO_2 heterostructure as a function phonon frequency. Gray points: all localized phonon modes in the MoS_2-a-SiO_2 heterostructure. Red points: phonon modes localized in MoS_2. Yellow circle: localized phonon mode corresponding to (f). Purple circle: localized phonon mode corresponding to (g).

The above atomistic level insights due to the vdW binding effects will lead to a device-level heat transfer optimization for the MoS_2-a-SiO_2 heterostructure. As shown in the inset of Figure 5a, an MoS_2 monolayer with radius L_s is supported by a 3D a-SiO_2 substrate. A hotspot with radius of δ was applied to the center of the MoS_2 monolayer, which represents a localized heat generation during the device operation. The hotspot size is typically scaled with the channel width of the device, which ranges from a few nanometers to several micrometers.[4,56–58] The characteristic length of the lateral heat spread L_h is thus given by,[19]

$$L_h = \sqrt{\frac{kt}{G}} \tag{2}$$

where t is the thickness of the MoS_2 monolayer. In this work, we chose t = 0.615 nm, which was determined by the neutron scattering experiment.[59] We defined $L_{h,0} \approx 80$ nm as the intrinsic lateral heat spread length, which corresponds to the condition of $\varepsilon'/\varepsilon = 1$. By leveraging the thermal transport properties given by MD simulations, we can calculate the vdW binding dependent overall heat transfer of this 2D-3D heterostructure device using a finite element simulation (see Supporting Information S8 for details about the simulation domain and

boundary conditions), where the fitting relationships for k and G shown in Figure 2 were used. A device-level thermal resistance R_p is defined based on the peak temperature of the hotspot T_{peak}, room temperature T_{room} (300 K), and the applied heating power q,[57,58]

$$R_p = \frac{T_{peak} - T_{room}}{q}. \quad (3)$$

Figure 5a shows the device thermal resistance R_p as a function of dimensionless binding energy ε'/ε for different MoS_2 monolayer radii. A hotspot with a radius of 25 nm was applied. With the increase of ε'/ε, R_p first decreases and then increases, leading to a minimum thermal resistance (denoted by a star for each condition). This optimal point is a result of the coupling of in-plane and cross-plane heat transfer. Specifically, when ε'/ε is small, L_h is larger than or comparable with δ (Eq. 2 and Figure S12 in Supporting Information S8), indicating that the heat can be sufficiently spread along the in-plane direction. For this reason, the overall heat transfer is mainly limited by the cross-plane heat transfer. With the increase of ε'/ε, the cross-plane thermal conductance G increases accordingly (Figure 2b), leading to the reduction of overall thermal resistance (marked as the G limited regime in Figure 5a). When ε'/ε increases further, L_h gradually becomes smaller than δ (Eq. 2 and Figure S12 in Supporting Information S8). Although G continues increasing with ε'/ε, the insufficient lateral heat spread due to the decrease of k and L_h becomes the limiting factor to the overall heat transfer, which leads to the increase of R_p (marked as the k limited regime in Figure 5a). When ε'/ε becomes sufficiently larger ($\varepsilon'/\varepsilon > 15$), the lateral heat spread is negligible (*i.e.*, $L_h \ll \delta$). The total area of the heat exchange between the MoS_2 monolayer and a-SiO_2 substrate is equal to the hotspot size. For this reason, R_p converges to the same value for different L_s (Figure 5a). In addition, the

minimum value of R_p depends on L_s. When L_s is comparable with L_h (*e.g.*, L_s = 50 nm and L_s = 100 nm in Figure 5a), the lateral heat spreading is significantly confined by the finite sample size. With the increase of L_s, as marked by the gray dash line in Figure 5a, the optimal value of R_p decreases accordingly. When L_s is much larger than L_h (*e.g.*, L_s = 250 nm and L_s = 500 nm in Figure 5a), the sample size is not a limiting factor for the lateral spread and R_p can reach its global optimal value (the purple star in Figure 5a).

A new heat transfer regime for the 2D-3D heterostructure can be observed by increasing the hotspot size. Figure 5b shows the device thermal resistance R_p as a function of dimensionless binding energy ε'/ε for different hotspot radii. The size of MoS_2 monolayer is sufficiently large (L_s = 3 μm), which does not confine the lateral heat spread. When the hotspot is highly localized (*i.e.*, δ = 25 nm and δ = 50 nm), the behavior of R_p is similar to the conditions shown in Figure 5a. However, when the hotspot size is sufficiently large (*i.e.*, δ = 100 nm and δ = 500 nm), R_p begins to monotonically decrease with ε'/ε and rapidly reaches a saturated value (marked as the yellow and purple stars in Figure 5b). This new regime arises from the value of $L_{h,0}$. When $L_{h,0}$ is larger than or comparable with δ, the overall heat transfer through the 2D-3D heterostructure is in an in-plane and cross-plane coupled regime (marked as G and k coupled in Figure 5b). For this reason, increasing ε'/ε leads to the transition from the cross-plane limited to the in-plane limited regime as shown in Figure 5a. However, if $L_{h,0}$ is smaller than δ, the lateral heat spread has already become insignificant without tuning the vdW binding energy. For this reason, the 2D-3D heterostructure enters a new regime, where the in-plane thermal conductivity is not important, and the overall heat transfer is determined by the cross-plane thermal conductance only (marked as the G dominated in Figure 5b). These heat transfer

regimes due to L_h, L_s, and δ are summarized in Table 1. Note that to show all possible regimes for a general 2D-3D heterostructure, the suppression of k due to the hotspot size effect was not considered in Figure 5.[60,61] However, a more realistic calculation by incorporating the suppression function of k (Figure S14) is shown in Figure S15 of the Supporting Information S8,[62] where a similar behavior of the overall heat transfer was shown. In general, the in-plane and cross-plane coupled regime can be more easily seen for a very high thermal conductivity 2D film (*e.g.*, graphene[63,64] and h-BN[65]) supported by an intrinsically weak vdW interface, whereas the cross-plane dominated regime is more common when a relatively low thermal conductivity 2D film (*e.g.*, transition metal dichalcogenides[20,44]) is strongly bonded by the bottom substrate. Different optimization strategies should be carried out by identifying the corresponding heat transfer regime for different 2D-3D heterostructures. In addition, although we increased ε'/ε up to 25 to span all possible conditions in the above analysis, our results show that reasonable tunability of vdW binding ($\varepsilon'/\varepsilon \approx$ 1-5) can already achieve the optimal heat transfer for various conditions, which is feasible for the practical applications. Note that for real 2D devices, the vdW interaction might also affect the carrier mobility and hence changes the heat generation rate, which requires further investigation in future works.

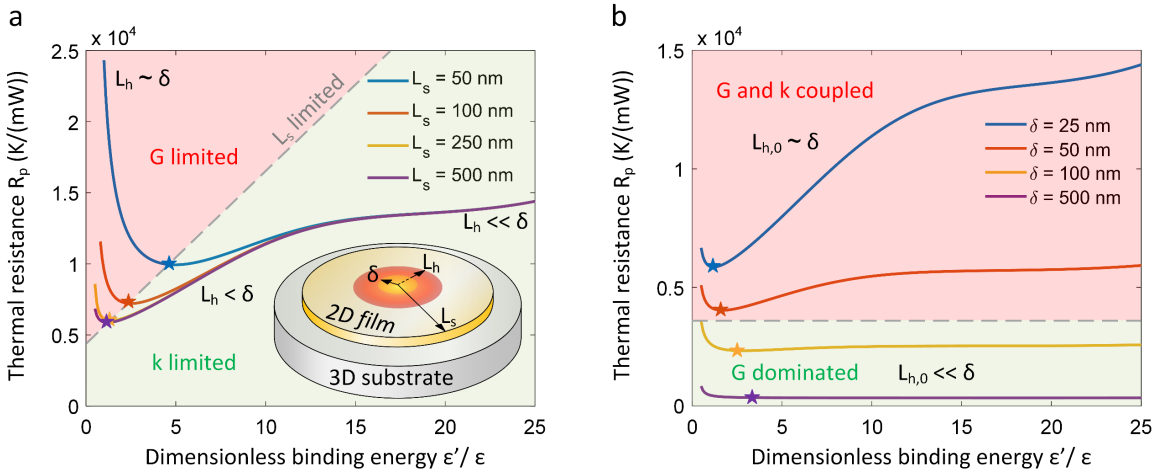

Figure 5. Thermal resistance as a function of vdW binding energy for the MoS_2-a-SiO_2 heterostructure with (a) different 2D film radii and (b) hotspot radii. When $L_{h,0}$ is larger than or comparable with δ, the device is in an in-plane and cross-plane coupled regime, where the overall heat transfer transitions from a G limited to a k limited state, leading to a minimum of R_p. When $L_{h,0}$ is much smaller than δ, the device is in a cross-plane dominated regime, where R_p monotonically decreases with ε'/ε.

Table 1. Summary of the device-level thermal transport characteristics through a 2D-3D vdW heterostructure.

Regime	Physics	Increase of ε'	Optimal ε' range
$\delta \sim L_{h,0}$	G and k coupled	$L_h \sim \delta$, G limited	L_s limited
		$L_h < \delta$, k limited	$\varepsilon'/\varepsilon \approx$ 1-5
$\delta \gg L_{h,0}$	G dominated	Monotonically decrease	$\varepsilon'/\varepsilon \approx$ 1-2

(Saturated point)

CONCLUSIONS

In summary, we investigated the vdW binding effects on heat transfer through a 2D-3D heterostructure by combining atomistic level insights with the device-level optimization. We calculated the in-plane thermal conductivity and cross-plane thermal conductance of an MoS_2-a-SiO_2 heterostructure using atomistic simulations. With the increase of vdW binding energy, we showed that the in-plane thermal conductivity decreases while the cross-plane thermal conductance increases, which was explained using the phonon relaxation time. When the vdW binding energy becomes significantly high ($\varepsilon'/\varepsilon > 10$), a saturating trend of the cross-plane thermal conductance, associated with several long relaxation time phonons, was observed. Using the phonon mode analysis based on SED and LD approaches, we showed that these long relaxation time phonons resulted from the vdW interaction-induced localized phonon modes. By leveraging the fundamental insights from atomistic simulations, we calculated the device-level heat transfer through the MoS_2-a-SiO_2 heterostructure. We showed the in-plane and cross-plane coupled and cross-plane dominated regimes for the device-level heat transfer, which are determined by the hotspot size, 2D film size, and lateral heat spread length. The vdW binding energy for the optimal thermal resistance was identified for each regime. This work elucidates the role of vdW interaction on the thermal transport through 2D-3D heterostructures, paving the way toward optimal thermal design of 2D nanoscale devices.

MATERIALS AND METHODS

MD simulation domain. MD simulation was performed using the LAMMPS package. A 6.2 nm × 5.4 nm area MoS_2-a-SiO_2 heterostructure was constructed. The thickness of a-SiO_2 substrate is 3.0 nm. Domain dependent analysis was carried out to ensure negligible size effects on the simulation results. Periodic boundary condition was applied along the in-plane direction. Details of the simulation domain, force field, domain size analysis, strain effect assessment, and EMD simulation can be seen in Supporting Information S1-S4.

Thermal conductivity calculation. Thermal conductivities of both the free-standing and substrate supported MoS_2 monolayers were calculated using the Green-Kubo formulism from EMD. The MoS_2-a-SiO_2 heterostructure was firstly equilibrated at 300 K in a constant pressure condition (NPT ensemble) for 1 ns, followed by a thermal relaxation in the canonical ensemble (NVT ensemble) for 1 ns and then a constant and constant volume ensemble (NVE ensemble) for 1 ns. Multiple simulations were performed, and the thermal conductivity was obtained from the average of multiple calculations. Each EMD simulation was conducted for 10 ns to ensure a reasonable convergence of the Green-Kubo formulism. Details of the EMD simulation can be seen in Supporting Information S1.

Thermal conductance calculation. The cross-plane thermal conductance was calculated using the approach-to-equilibrium molecular dynamics. A thermal circuit was constructed to describe the transient thermal response of the MoS_2-a-SiO_2 heterostructure. This thermal circuit consists of a MoS_2 thermal capacitors, a SiO_2 thermal capacitor, and a thermal resistor, which is the inverse of the interfacial thermal conductance. The capacitance of MoS_2 monolayer and a-SiO_2

substrate were determined by their heat capacities and atom masses. Heat capacities for the same simulated material system were calculated using EMD. The MoS_2-a-SiO_2 heterostructure was firstly equilibrated at 300 K for 1 ns in a constant pressure condition (NPT ensemble), followed by a constant volume condition (NVT ensemble) for 1 ns. A 200 K temperature rise was then created on the MoS_2 monolayer and the MoS_2-a-SiO_2 heterostructure was placed in a constant energy and constant volume condition (NVE ensemble). The interfacial thermal conductance was determined by fitting the transient temperature decay. Details of the approach-to-equilibrium approach, heat capacities calculations, and fitting approach can be seen in Supporting Information S1 and S3.

Phonon relaxation time. We calculated the phonon relaxation time using SED analysis. In each SED calculation, the MoS_2-a-SiO_2 was relaxed the same as the EMD simulation. The phonon relaxation time was determined by the linewidth of the SED peak. We fitted each peak in the SED spectra using Lorentzian function. The phonon relaxation times of 81 **k**-points in the first quadrant of 2D BLZ were calculated. The acoustic modes and optical modes were distinguished by the phonon bandgap of MoS_2 monolayer. Details of phonon relaxation time calculation and SED analysis can be seen in Supporting Information S1.

vdW force spectrum. The real-time variation of vdW force between MoS_2 monolayer and a-SiO_2 substrate during 1 ns EMD simulation was recorded. The vdW force spectrum was obtained by performing Fourier transform to the time-domain vdW force. Details of vdW force spectrum calculation can be seen in Supporting Information S5.

Localized phonon and participation ratio. We performed the phonon mode analysis for the

entire MoS_2-a-SiO_2 heterostructure using GULP. The force field for LD calculation was the same as the MD simulation. The eigenvector for each atom and vibrational mode was identified from LD. We calculated the participation ratio of each vibrational mode and determined the localized modes. The localized phonons in MoS_2 were defined as the modes (1) with less than 0.1 participation ratio and (2) the largest component of eigenvector in the MoS_2 monolayer. Details of LD analysis and participation ratio calculation can be seen in Supporting Information S6 and S7.

Device-level thermal transport. Finate element simulation was performed to quantify the device-level thermal transport in COMSOL Multiphysics. An axisymmetric MoS_2-a-SiO_2 heterostructure was created with the MD determined thermal conductivity and interfacial thermal conductance as the input. A hotspot was placed at the center of the heterostructure whereas the rest area of the MoS_2 monolayer was exposed to the ambient air with a convective heat transfer coefficient of 10 W/(m^2K). The bottom of the a-SiO_2 substrate was prescribed as a constant temperature of 20 ℃. The device-level thermal resistance was calculated by solving the Fourier conduction equation with various hotspot sizes, MoS_2 sample sizes, and vdW binding energies. Impact of the quasiballistic phonon transport due to the nanoscale size of hotspot was also evaluated using an effective thermal conductivity given by a radical suppression function. Details of the computational domain, boundary conditions, simulation parameters, effective thermal conductivity, and radical suppression function can be seen in Supporting Information S8.

ASSOCIATED CONTENT

Supporting Information

The Supporting Information is available free of charge on the ACS Publications website at DOI:

Molecular dynamics simulations for thermal transport properties at the equilibrium; parameters for Lenard-Jones (LJ) potentials from universal force field (UFF); thermal circuit – approach to equilibrium molecular dynamics simulation; size dependence of thermal properties in MD simulation; frequency-domain analysis of cross-plane heat flux and vdW force; lattice dynamics calculation for vibrational mode analysis; vdW binding effects on phonon group velocity and phonon density of state (PDOS); finite element analysis for device-level optimization.

AUTHOR INFORMATION

Corresponding Authors

* E-mail: guol3@sustech.edu.cn

* E-mail: gchen2@mit.edu

* E-mail: enwang@mit.edu

Author Contributions

# L.Z. and Y.Z. contributed equally to this work.

Notes

The authors declare no competing financial interest.

ACKNOWLEDGMENTS

The authors gratefully acknowledge the funding support from the Centers for Mechanical Engineering Research and Education at MIT and SUSTech. The authors also gratefully acknowledge the Extreme Science and Engineering Discovery Environment (XSEDE) supported by National Science Foundation for use of computing resources. This work used XSEDE Stampede2 at the Texas Advanced Computing Center (TACC) through allocation TG-ECS190012 and TG-DMR190125. L.Z. acknowledges the funding support from MIT Martin Family Society of Fellows for Sustainability, Abdul Latif Jameel Water and Food Systems Lab (J-WAFS), and Singapore-MIT Alliance for Research and Technology (SMART) LEES Program.

REFERENCES

(1) Wang, Q. H.; Kalantar-Zadeh, K.; Kis, A.; Coleman, J. N.; Strano, M. S. Electronics and Optoelectronics of Two-Dimensional Transition Metal Dichalcogenides. *Nat. Nanotechnol.* **2012**, *7* (11), 699–712.

(2) Butler, S. Z.; Hollen, S. M.; Cao, L.; Cui, Y.; Gupta, J. A.; Gutiérrez, H. R.; Heinz, T. F.; Hong, S. S.; Huang, J.; Ismach, A. F.; Johnston-Halperin, E.; Kuno, M.; Plashnitsa, V.

V.; Robinson, R. D.; Ruoff, R. S.; Salahuddin, S.; Shan, J.; Shi, L.; Spencer, M. G.; Terrones, M.; Windl, W.; Goldberger, J. E. Progress, Challenges, and Opportunities in Two-Dimensional Materials Beyond Graphene. *ACS Nano* **2013**, *7* (4), 2898–2926.

(3) Sarkar, D.; Xie, X.; Liu, W.; Cao, W.; Kang, J.; Gong, Y.; Kraemer, S.; Ajayan, P. M.; Banerjee, K. A Subthermionic Tunnel Field-Effect Transistor with an Atomically Thin Channel. *Nature* **2015**, *526* (7571), 91–95.

(4) Nourbakhsh, A.; Zubair, A.; Sajjad, R. N.; Tavakkoli K. G., A.; Chen, W.; Fang, S.; Ling, X.; Kong, J.; Dresselhaus, M. S.; Kaxiras, E.; Berggren, K. K.; Antoniadis, D.; Palacios, T. MoS_2 Field-Effect Transistor with Sub-10 Nm Channel Length. *Nano Lett.* **2016**, *16* (12), 7798–7806.

(5) Chen, M.-L.; Sun, X.; Liu, H.; Wang, H.; Zhu, Q.; Wang, S.; Du, H.; Dong, B.; Zhang, J.; Sun, Y.; Qiu, S.; Alava, T.; Liu, S.; Sun, D.-M.; Han, Z. A FinFET with One Atomic Layer Channel. *Nat. Commun.* **2020**, *11* (1), 1205.

(6) Pesin, D.; MacDonald, A. H. Spintronics and Pseudospintronics in Graphene and Topological Insulators. *Nat. Mater.* **2012**, *11* (5), 409–416.

(7) Luo, Y. K.; Xu, J.; Zhu, T.; Wu, G.; McCormick, E. J.; Zhan, W.; Neupane, M. R.; Kawakami, R. K. Opto-Valleytronic Spin Injection in Monolayer MoS_2/Few-Layer Graphene Hybrid Spin Valves. *Nano Lett.* **2017**, *17* (6), 3877–3883.

(8) Behura, S. K.; Wang, C.; Wen, Y.; Berry, V. Graphene–Semiconductor Heterojunction Sheds Light on Emerging Photovoltaics. *Nat. Photonics* **2019**, *13* (5), 312–318.

(9) Bernardi, M.; Palummo, M.; Grossman, J. C. Extraordinary Sunlight Absorption and One Nanometer Thick Photovoltaics Using Two-Dimensional Monolayer Materials. *Nano Lett.* **2013**, *13* (8), 3664–3670.

(10) He, Y.-M.; Clark, G.; Schaibley, J. R.; He, Y.; Chen, M.-C.; Wei, Y.-J.; Ding, X.; Zhang, Q.; Yao, W.; Xu, X.; Lu, C.-Y.; Pan, J.-W. Single Quantum Emitters in Monolayer Semiconductors. *Nat. Nanotechnol.* **2015**, *10* (6), 497–502.

(11) Chang, T.-Y.; Chen, Y.; Luo, D.-I.; Li, J.-X.; Chen, P.-L.; Lee, S.; Fang, Z.; Li, W.-Q.; Zhang, Y.-Y.; Li, M.; Majumdar, A.; Liu, C.-H. Black Phosphorus Mid-Infrared Light-Emitting Diodes Integrated with Silicon Photonic Waveguides. *Nano Lett.* **2020**, *20* (9), 6824–6830.

(12) Freitag, M.; Chiu, H.-Y.; Steiner, M.; Perebeinos, V.; Avouris, P. Thermal Infrared Emission from Biased Graphene. *Nat. Nanotechnol.* **2010**, *5* (7), 497–501.

(13) Ong, Z.-Y.; Bae, M.-H. Energy Dissipation in van Der Waals 2D Devices. *2D Mater.* **2019**, *6* (3), 032005.

(14) Yalon, E.; McClellan, C. J.; Smithe, K. K. H.; Muñoz Rojo, M.; Xu, R. L.; Suryavanshi, S. V.; Gabourie, A. J.; Neumann, C. M.; Xiong, F.; Farimani, A. B.; Pop, E. Energy Dissipation in Monolayer MoS_2 Electronics. *Nano Lett.* **2017**, *17* (6), 3429–3433.

(15) Bae, M.-H.; Islam, S.; Dorgan, V. E.; Pop, E. Scaling of High-Field Transport and Localized Heating in Graphene Transistors. *ACS Nano* **2011**, *5* (10), 7936–7944.

(16) Zhang, L.; Lu, Z.; Song, Y.; Zhao, L.; Bhatia, B.; Bagnall, K. R.; Wang, E. N. Thermal

Expansion Coefficient of Monolayer Molybdenum Disulfide Using Micro-Raman Spectroscopy. *Nano Lett.* **2019**, *19* (7), 4745–4751.

(17) Yoon, D.; Son, Y.-W.; Cheong, H. Negative Thermal Expansion Coefficient of Graphene Measured by Raman Spectroscopy. *Nano Lett.* **2011**, *11* (8), 3227–3231.

(18) Sood, A.; Xiong, F.; Chen, S.; Cheaito, R.; Lian, F.; Asheghi, M.; Cui, Y.; Donadio, D.; Goodson, K. E.; Pop, E. Quasi-Ballistic Thermal Transport Across MoS_2 Thin Films. *Nano Lett.* **2019**, *19* (4), 2434–2442.

(19) Yalon, E.; Aslan, Ö. B.; Smithe, K. K. H.; McClellan, C. J.; Suryavanshi, S. V.; Xiong, F.; Sood, A.; Neumann, C. M.; Xu, X.; Goodson, K. E.; Heinz, T. F.; Pop, E. Temperature-Dependent Thermal Boundary Conductance of Monolayer MoS_2 by Raman Thermometry. *ACS Appl. Mater. Interfaces* **2017**, *9* (49), 43013–43020.

(20) Zhang, X.; Sun, D.; Li, Y.; Lee, G.-H.; Cui, X.; Chenet, D.; You, Y.; Heinz, T. F.; Hone, J. C. Measurement of Lateral and Interfacial Thermal Conductivity of Single- and Bilayer MoS_2 and $MoSe_2$ Using Refined Optothermal Raman Technique. *ACS Appl. Mater. Interfaces* **2015**, *7* (46), 25923–25929.

(21) Foss, C. J.; Aksamija, Z. Quantifying Thermal Boundary Conductance of 2D–3D Interfaces. *2D Mater.* **2019**, *6* (2), 025019.

(22) Suryavanshi, S. V.; Gabourie, A. J.; Barati Farimani, A.; Pop, E. Thermal Boundary Conductance of Two-Dimensional MoS_2 Interfaces. *J. Appl. Phys.* **2019**, *126* (5), 055107.

(23) Zhang, J.; Hong, Y.; Liu, M.; Yue, Y.; Xiong, Q.; Lorenzini, G. Molecular Dynamics Simulation of the Interfacial Thermal Resistance between Phosphorene and Silicon Substrate. *Int. J. Heat Mass Transf.* **2017**, *104*, 871–877.

(24) Sun, L.; Banhart, F.; Krasheninnikov, A. V.; Rodriguez-Manzo, J. A.; Terrones, M.; Ajayan, P. M. Carbon Nanotubes as High-Pressure Cylinders and Nanoextruders. *Science* **2006**, *312* (5777), 1199–1202.

(25) Tang, J.; Qin, L.-C.; Sasaki, T.; Yudasaka, M.; Matsushita, A.; Iijima, S. Compressibility and Polygonization of Single-Walled Carbon Nanotubes under Hydrostatic Pressure. *Phys. Rev. Lett.* **2000**, *85* (9), 1887–1889.

(26) Ci, P.; Chen, Y.; Kang, J.; Suzuki, R.; Choe, H. S.; Suh, J.; Ko, C.; Park, T.; Shen, K.; Iwasa, Y.; Tongay, S.; Ager, J. W.; Wang, L.-W, Wu, J. Quantifying van Der Waals Interactions in Layered Transition Metal Dichalcogenides from Pressure-Enhanced Valence Band Splitting. *Nano Lett.* **2017**, *17* (8), 4982–4988.

(27) Yankowitz, M.; Jung, J.; Laksono, E.; Leconte, N.; Chittari, B. L.; Watanabe, K.; Taniguchi, T.; Adam, S.; Graf, D.; Dean, C. R. Dynamic Band-Structure Tuning of Graphene Moiré Superlattices with Pressure. *Nature* **2018**, *557* (7705), 404–408.

(28) Hohensee, G. T.; Wilson, R. B.; Cahill, D. G. Thermal Conductance of Metal–Diamond Interfaces at High Pressure. *Nat. Commun.* **2015**, *6* (1), 6578.

(29) Pak, S.; Lee, J.; Lee, Y.-W.; Jang, A.-R.; Ahn, S.; Ma, K. Y.; Cho, Y.; Hong, J.; Lee, S.; Jeong, H. Y.; Im, H.; Shin, H. S.; Morris, S. M.; Cha, S.; Sohn, J. I.; Kim, J. M. Strain-

Mediated Interlayer Coupling Effects on the Excitonic Behaviors in an Epitaxially Grown MoS_2/WS_2 van Der Waals Heterobilayer. *Nano Lett.* **2017**, *17* (9), 5634–5640.

(30) Muruganathan, M.; Sun, J.; Imamura, T.; Mizuta, H. Electrically Tunable van Der Waals Interaction in Graphene–Molecule Complex. *Nano Lett.* **2015**, *15* (12), 8176–8180.

(31) Huttmann, F.; Martínez-Galera, A. J.; Caciuc, V.; Atodiresei, N.; Schumacher, S.; Standop, S.; Hamada, I.; Wehling, T. O.; Blügel, S.; Michely, T. Tuning the van Der Waals Interaction of Graphene with Molecules via Doping. *Phys. Rev. Lett.* **2015**, *115* (23), 236101.

(32) Lessel, M.; Loskill, P.; Hausen, F.; Gosvami, N. N.; Bennewitz, R.; Jacobs, K. Impact of van Der Waals Interactions on Single Asperity Friction. *Phys. Rev. Lett.* **2013**, *111* (3), 035502.

(33) Meng, X.; Pandey, T.; Jeong, J.; Fu, S.; Yang, J.; Chen, K.; Singh, A.; He, F.; Xu, X.; Zhou, J.; Hsieh, W.-P.; Singh, A. K.; Lin, J.-F.; Wang, Y. Thermal Conductivity Enhancement in MoS_2 under Extreme Strain. *Phys. Rev. Lett.* **2019**, *122* (15), 155901.

(34) Plimpton, S. Fast Parallel Algorithms for Short-Range Molecular Dynamics. *J. Comput. Phys.* **1995**, *117* (1), 1–19.

(35) Jiang, J.-W. Parametrization of Stillinger–Weber Potential Based on Valence Force Field Model: Application to Single-Layer MoS_2 and Black Phosphorus. *Nanotechnology* **2015**, *26* (31), 315706.

(36) Munetoh, S.; Motooka, T.; Moriguchi, K.; Shintani, A. Interatomic Potential for Si–O

Systems Using Tersoff Parameterization. *Comput. Mater. Sci.* **2007**, *39* (2), 334–339.

(37) Rappe, A. K.; Casewit, C. J.; Colwell, K. S.; Goddard, W. A.; Skiff, W. M. UFF, a Full Periodic Table Force Field for Molecular Mechanics and Molecular Dynamics Simulations. *J. Am. Chem. Soc.* **1992**, *114* (25), 10024–10035.

(38) Volz, S. G.; Chen, G. Molecular-Dynamics Simulation of Thermal Conductivity of Silicon Crystals. *Phys. Rev. B* **2000**, *61* (4), 2651–2656.

(39) Henry, A.; Chen, G. High Thermal Conductivity of Single Polyethylene Chains Using Molecular Dynamics Simulations. *Phys. Rev. Lett.* **2008**, *101* (23), 235502.

(40) Xu, K.; Gabourie, A. J.; Hashemi, A.; Fan, Z.; Wei, N.; Farimani, A. B.; Komsa, H.-P.; Krasheninnikov, A. V.; Pop, E.; Ala-Nissila, T. Thermal Transport in MoS_2 from Molecular Dynamics Using Different Empirical Potentials. *Phys. Rev. B* **2019**, *99* (5), 054303.

(41) Gabourie, A. J.; Suryavanshi, S. V.; Farimani, A. B.; Pop, E. Reduced Thermal Conductivity of Supported and Encased Monolayer and Bilayer MoS2. *2D Mater.* **2021**, *8*, 011001.

(42) Gu, X.; Li, B.; Yang, R. Layer Thickness-Dependent Phonon Properties and Thermal Conductivity of MoS_2. *J. Appl. Phys.* **2016**, *119* (8), 085106.

(43) Gandi, A. N.; Schwingenschlögl, U. Thermal Conductivity of Bulk and Monolayer MoS_2. *Europhys. Lett.* **2016**, *113* (3), 36002.

(44) Yang, X.; Zheng, X.; Liu, Q.; Zhang, T.; Bai, Y.; Yang, Z.; Chen, H.; Liu, M.

Experimental Study on Thermal Conductivity and Rectification in Suspended Monolayer MoS_2. *ACS Appl. Mater. Interfaces* **2020**, *12* (25), 28306–28312.

(45) Hahn, K. R.; Puligheddu, M.; Colombo, L. Thermal Boundary Resistance at Si/Ge Interfaces Determined by Approach-to-Equilibrium Molecular Dynamics Simulations. *Phys. Rev. B* **2015**, *91* (19), 195313.

(46) Feng, T.; Ruan, X. Prediction of Spectral Phonon Mean Free Path and Thermal Conductivity with Applications to Thermoelectrics and Thermal Management: A Review. *J. Nanomater.* **2014**, *2014*, 1–25.

(47) Seyf, H. R.; Henry, A. A Method for Distinguishing between Propagons, Diffusions, and Locons. *J. Appl. Phys.* **2016**, *120* (2), 025101.

(48) Chen, G. *Nanoscale Energy Transport and Conversion: A Parallel Treatment of Electrons, Molecules, Phonons, and Photons*; MIT-Pappalardo Series in Mechanical Engineering; Oxford University Press, 2005.

(49) Feng, T.; Qiu, B.; Ruan, X. Anharmonicity and Necessity of Phonon Eigenvectors in the Phonon Normal Mode Analysis. *J. Appl. Phys.* **2015**, *117* (19), 195102.

(50) Qiu, B.; Ruan, X. Reduction of Spectral Phonon Relaxation Times from Suspended to Supported Graphene. *Appl. Phys. Lett.* **2012**, *100* (19), 193101.

(51) Feng, T.; Yao, W.; Wang, Z.; Shi, J.; Li, C.; Cao, B.; Ruan, X. Spectral Analysis of Nonequilibrium Molecular Dynamics: Spectral Phonon Temperature and Local Nonequilibrium in Thin Films and across Interfaces. *Phys. Rev. B* **2017**, *95* (19), 195202.

(52) Gale, J. D. GULP: A Computer Program for the Symmetry-Adapted Simulation of Solids. *J. Chem. Soc. Faraday Trans.* **1997**, *93* (4), 629–637.

(53) Zhu, T.; Ertekin, E. Phonons, Localization, and Thermal Conductivity of Diamond Nanothreads and Amorphous Graphene. *Nano Lett.* **2016**, *16* (8), 4763–4772.

(54) Seyf, H. R.; Yates, L.; Bougher, T. L.; Graham, S.; Cola, B. A.; Detchprohm, T.; Ji, M.-H.; Kim, J.; Dupuis, R.; Lv, W.; Henry, A. Rethinking Phonons: The Issue of Disorder. *npj Comput. Mater.* **2017**, *3* (1), 49.

(55) Yang, J.; Qian, X.; Pan, W.; Yang, R.; Li, Z.; Han, Y.; Zhao, M.; Huang, M.; Wan, C. Diffused Lattice Vibration and Ultralow Thermal Conductivity in the Binary Ln–Nb–O Oxide System. *Adv. Mater.* **2019**, *31* (24), 1808222.

(56) Brault, J.; Saitoh, M.; Hiramoto, T. Channel Width and Length Dependence in Si Nanocrystal Memories With Ultra-Nanoscale Channel. *IEEE Trans. Nanotechnol.* **2005**, *4* (3), 349–354.

(57) Bagnall, K. R.; Moore, E. A.; Badescu, S. C.; Zhang, L.; Wang, E. N. Simultaneous Measurement of Temperature, Stress, and Electric Field in GaN HEMTs with Micro-Raman Spectroscopy. *Rev. Sci. Instrum.* **2017**, *88* (11), 113111.

(58) Foy, C.; Zhang, L.; Trusheim, M. E.; Bagnall, K. R.; Walsh, M.; Wang, E. N.; Englund, D. R. Wide-Field Magnetic Field and Temperature Imaging Using Nanoscale Quantum Sensors. *ACS Appl. Mater. Interfaces* **2020**, *12* (23), 26525–26533.

(59) Wakabayashi, N.; Smith, H. G.; Nicklow, R. M. Lattice Dynamics of Hexagonal MoS_2

Studied by Neutron Scattering. *Phys. Rev. B* **1975**, *12* (2), 659–663.

(60) Minnich, A. J.; Johnson, J. A.; Schmidt, A. J.; Esfarjani, K.; Dresselhaus, M. S.; Nelson, K. A.; Chen, G. Thermal Conductivity Spectroscopy Technique to Measure Phonon Mean Free Paths. *Phys. Rev. Lett.* **2011**, *107* (9), 095901.

(61) Hu, Y.; Zeng, L.; Minnich, A. J.; Dresselhaus, M. S.; Chen, G. Spectral Mapping of Thermal Conductivity through Nanoscale Ballistic Transport. *Nat. Nanotechnol.* **2015**, *10* (8), 701–706.

(62) Ding, D.; Chen, X.; Minnich, A. J. Radial Quasiballistic Transport in Time-Domain Thermoreflectance Studied Using Monte Carlo Simulations. *Appl. Phys. Lett.* **2014**, *104* (14), 143104.

(63) Balandin, A. A.; Ghosh, S.; Bao, W.; Calizo, I.; Teweldebrhan, D.; Miao, F.; Lau, C. N. Superior Thermal Conductivity of Single-Layer Graphene. *Nano Lett.* **2008**, *8* (3), 902–907.

(64) Cai, W.; Moore, A. L.; Zhu, Y.; Li, X.; Chen, S.; Shi, L.; Ruoff, R. S. Thermal Transport in Suspended and Supported Monolayer Graphene Grown by Chemical Vapor Deposition. *Nano Lett.* **2010**, *10* (5), 1645–1651.

(65) Cai, Q.; Scullion, D.; Gan, W.; Falin, A.; Zhang, S.; Watanabe, K.; Taniguchi, T.; Chen, Y.; Santos, E. J. G.; Li, L. H. High Thermal Conductivity of High-Quality Monolayer Boron Nitride and Its Thermal Expansion. *Sci. Adv.* **2019**, *5* (6), eaav0129.

TOC Graphic (3.25 in × 1.75 in, 600 dpi)